JACS
JOURNAL OF THE AMERICAN CHEMICAL SOCIETY
pubs.acs.org/JACS
Article

Atomic Insight into the Local Structure and Microenvironment of Isolated Co-Motifs in MFI Zeolite Frameworks for Propane Dehydrogenation

Zhong-Pan Hu,[▽] Gangqiang Qin,[▽] Jingfeng Han, Wenna Zhang, Nan Wang, Yijun Zheng, Qike Jiang, Te Ji, Zhong-Yong Yuan, Jianping Xiao,* Yingxu Wei,* and Zhongmin Liu*

Cite This: J. Am. Chem. Soc. 2022, 144, 12127−12137

Read Online

ACCESS | Metrics & More | Article Recommendations | Supporting Information

ABSTRACT: Embedding metal species into zeolite frameworks can create framework-bond metal sites in a confined microenvironment. The metals sitting in the specific T sites of zeolites and their crystalline surroundings are both committed to the interaction with the reactant, participation in the activation, and transient state achievement during the whole catalytic process. Herein, we construct isolated Co-motifs into purely siliceous MFI zeolite frameworks (Co-MFI) and reveal the location and microenvironment of the isolated Co active center in the MFI zeolite framework particularly beneficial for propane dehydrogenation (PDH). The isolated Co-motif with the distorted tetrahedral structure ($\{(\equiv SiO)_2Co(HO-Si\equiv)_2\}$, two Co−O−Si bonds, and two pseudo-bridging hydroxyls (Co···OH−Si) is located at $T_{1(7)}$ and $T_{3(9)}$ sites of the MFI zeolite. DFT calculations and deuterium-labeling reactions verify that the isolated Co-motif together with the MFI microenvironment collectively promotes the PDH reaction by providing an exclusive microenvironment to preactivate C_3H_8, polarizing the oxygen in Co−O−Si bonds to accept H* ($\{(\equiv SiO)CoH^{\delta-}(H^{\delta+}O-Si\equiv)_3\}$), and a scaffold structure to stabilize the C_3H_7* intermediate. The Co-motif active center in Co-MFI goes through the dynamic evolutions and restoration in electronic states and coordination states in a continuous and repetitive way, which meets the requirements from the series of elementary steps in the PDH catalytic cycle and fulfills the successful catalysis like enzyme catalysis.

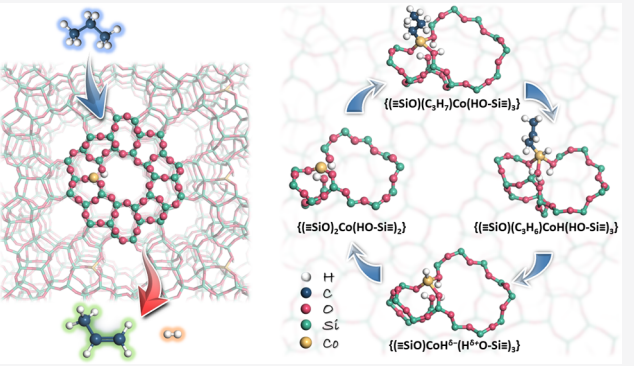

INTRODUCTION

The introduction of metallic active centers into porous materials, especially zeolites to form metal−zeolite materials, has achieved great success in catalytic applications such as dehydrogenation,[1,2] hydrogenation,[3,4] and oxidation.[5,6] A growing consensus is that the zeolite catalysis in a specific reaction depends not only on the active sites located in the zeolite but also on the microenvironment surrounding the protonic or metallic centers.[7−10] The confined nanospace close to the guest molecular size can provide a promising and fascinating space for reactant activation and transformation. These advantages should also be reflected in the metallic species-introduced zeolite materials and their applications. This kind of introduction would unconsciously imitate some of the characteristics of enzyme catalysis.[11,12] Through the synergistic effect of metallic active sites and the reaction microenvironment, the constructed metal−zeolite catalytic system helps the reactants to be adsorbed, be activated, reach the transition state, and generate products, therefore realizing the catalytic cycle in an optimized reaction pathway in some typical reactions, such as alkane activation with strong potential, which is a necessity for industrial applications.[13−17]

The combination of metallic species and zeolites has contributed to the development of important catalysts, for example, Fe-BEA,[14−16] Cu-CHA,[13,18] and Rh-ZSM-5.[19] With zeolites as the support, metal species are encapsulated inside or highly dispersed on the zeolite surface resulting in nano- or subnano-scale metal particles, which are responsible for the high efficiency and long-life reaction performance of alkane dehydrogenation.[20−22] In other cases, researchers are seeking to embed metal species into zeolite frameworks to form heteroatomic zeolites. This kind of incorporation realizes atomic-level metallic species dispersion and produces a

Received: March 10, 2022
Published: June 28, 2022

https://doi.org/10.1021/jacs.2c02636
J. Am. Chem. Soc. 2022, 144, 12127−12137

uniform metal−zeolite material with metal atoms sitting in the tetrahedrally coordinated frameworks. To date, several heteroatomic metal−zeolites have been synthesized and used for industrial applications, such as titanium silicalite (TS-1) for olefin epoxidation[5,6] and Sn-Beta for carbohydrate conversion into platform and commodity chemicals.[23,24] However, the incorporation of some other transition metal atoms (e.g., Co, Ni, and Cu) selectively into a specific position of the zeolite framework is still very difficult owing to the steric constraints of zeolites and problematic host−guest matching between metallic species and zeolites. Usually, nanoparticles with a size larger than 0.5 nm would be formed in or on zeolites during the synthesis procedure.[25,26] So far, the introduction of single transition metallic atoms within the desired framework or channel of zeolites is still a challenging and cutting-edge technology in the exploitation of functional metal−zeolite catalysts.

Recently, cobalt (Co)-containing catalysts have been reported to be active for alkane dehydrogenation.[27−32] Typically, the diversity of supports and preparation methods employed for Co-containing catalyst construction would result in the diversity of Co species and further significantly affect the alkane dehydrogenation performance. The presence of various Co species, e.g., isolated Co, cluster, and nanoparticle CoO_x caused controversy about the metallic active sites. Employing zeolites as the environment to accommodate Co sites is a promising approach to achieve a uniform Co−zeolite catalytic system for efficient conversion, as well as for the structure definition, acid site identification, and catalysis understanding.[33,34] For a long time, high-angle annular dark-field scanning transmission electron microscopy (HAADF-STEM) has been used to identify metallic sites in zeolites but has been seriously restricted to identify the light atoms in the zeolite framework.[35,36] Alternatively, integrated differential phase-contrast scanning transmission electron microscopy (iDPC-STEM) has exhibited unique advantages in the identification of heteroatoms within zeolites, as a result of its sufficient and interpretable image contrast for light elements under low-dose conditions.[37−39] In addition, other multiple technologies, e.g., X-ray absorption spectroscopy (XAS),[13,19,20] FTIR spectroscopy,[13,19] and UV−visible spectroscopy,[3,5,14] combined with theoretical calculations,[13−15,18,20] help to understand the structure and reaction mechanism of the metal−zeolite system.

Based on the above considerations, the Co-MFI catalyst with atomically dispersed Co species embedded into the MFI zeolite framework was constructed through the ligand-protected hydrothermal synthesis method. The location and structure of Co active centers were identified by combining iDPC-STEM, XAS, and FTIR spectroscopy, revealing a homogeneous distribution of single Co sites in the MFI framework with a distorted tetrahedra-coordination state. Co-MFI was used for the propane dehydrogenation (PDH) reaction, exhibiting excellent performance. Through density functional theory (DFT) calculations including the projected density of states (PDOS) and charge analysis, together with deuterium-labeling experiments, the active site of Co-MFI was identified and the PDH reaction mechanism was proposed. The unique catalytic microenvironment with Co sites embedded into the MFI framework and the zeolite surrounding could collectively participate in promoting propane activation and dehydrogenation and are responsible for the highly efficient conversion.

RESULTS AND DISCUSSION

Construction of Co-MFI Zeolites. In this work, we construct Co-MFI zeolites and present direct evidence for single Co atoms embedding into the purely siliceous MFI zeolite framework. Typically, the Co-MFI zeolites were prepared by the ligand-protected hydrothermal synthesis method starting from the gel of $1SiO_2$:nCoO:$2n$ETD (ethanediamine):0.3TPAOH (tetrapropylammonium hydroxide):4IPA (isopropanol):$35H_2O$ (n = 0.03, 0.05, 1.0, 2.0, and 3.0). Due to the coordination interaction between Co and ETD, Co species in the form of Co(II)-ETD complexes are in situ embedded into the siliceous MFI framework during the crystallization process (Figure S1 and Table S1). By optimizing the synthesis conditions, Co-MFI with 1.12 wt % Co content is selected as the representative material. The XRD patterns of Co-MFI exhibit typical diffraction peaks, characteristic of the MFI framework (Figure S2). C_s-corrected HAADF-STEM (Figure S3) and iDPC-STEM images (Figure 1a−f) of Co-MFI taken along three main crystallographic axes display that the Co-MFI zeolite possesses good crystallinity and well-defined MFI topological structure without any clusters and nanoparticles. Since the framework Co and Si atoms are difficult to be distinguished by HAADF-STEM under the low-electron dose conditions to keep the zeolite structure (Figure 1g), accordingly, iDPC-STEM technology is employed to disclose them (Figure 1h−k). In Figure 1h, some brighter white dots sitting in T sites of the MFI lattice, circled in yellow, can be distinguished as the framework Co atoms from other framework atoms in the MFI zeolite. The enlarged images of three typical local structures are provided in Figure 1i−k: the

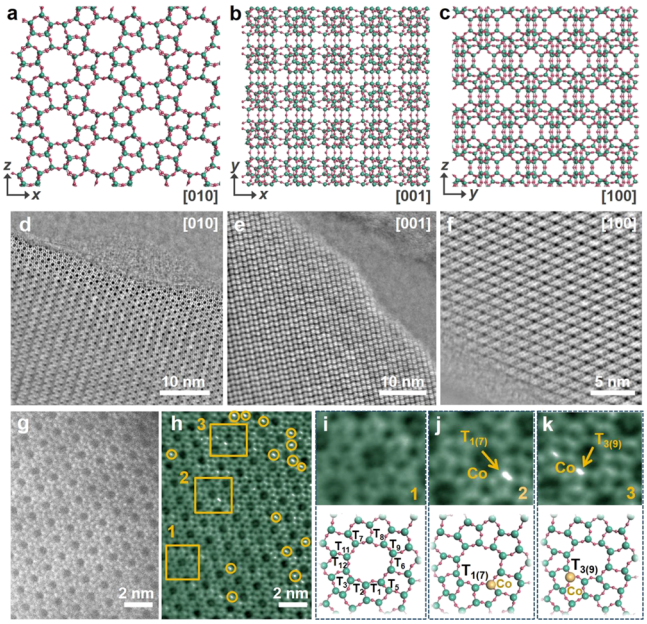

Figure 1. Electron microscopy analyses of the Co-MFI zeolite with a Co content of 1.12 wt %. (a−c) Structure of the MFI-type framework. (d−f) C_s-corrected iDPC-STEM images of the Co-MFI framework were taken along the three main crystallographic axes. (g) C_s-corrected HAADF-STEM image and (h) corresponding iDPC-STEM image of the Co-MFI framework. (k−m) Zoomed-in areas of 1, 2, and 3 in (h), respectively: the MFI framework without Co (i) and the MFI framework containing Co at the $T_{1(7)}$ site (j) and the $T_{3(9)}$ site (k).

https://doi.org/10.1021/jacs.2c02636
J. Am. Chem. Soc. 2022, 144, 12127−12137

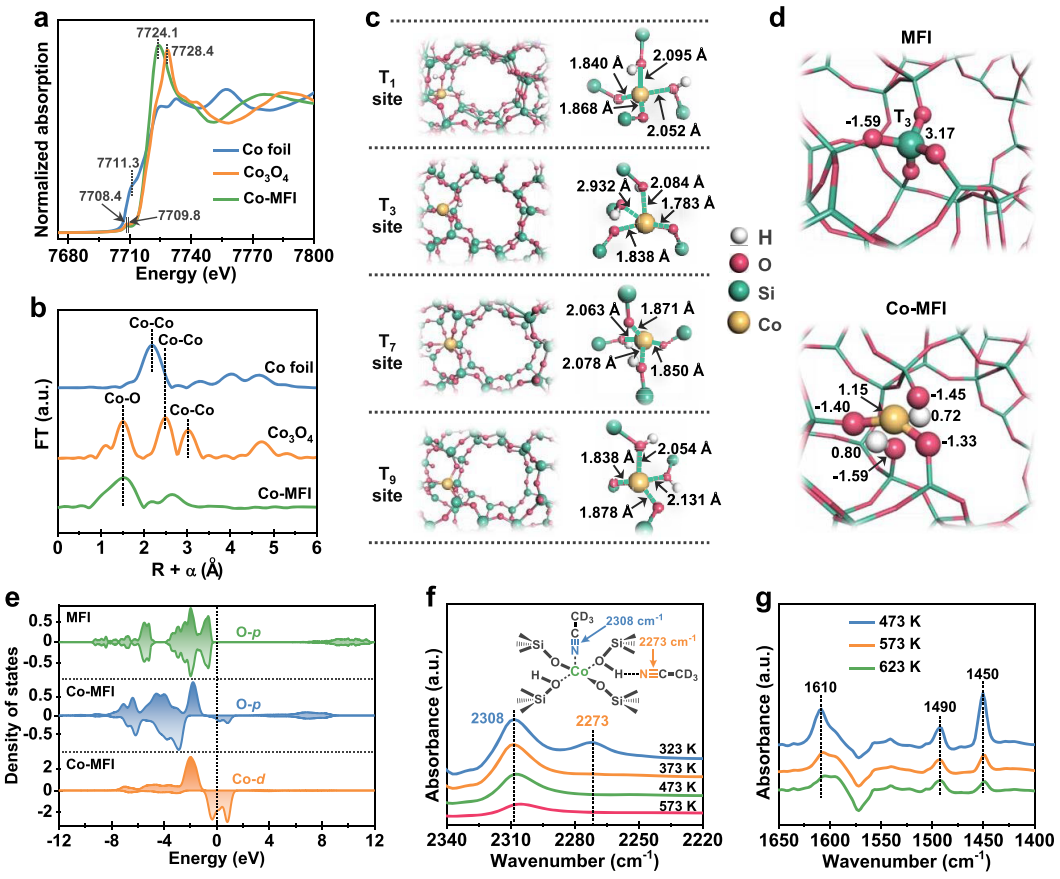

Figure 2. Structure of Co-MFI. (a) Co K-edge XANES spectra and (b) corresponding FT k^3-weighted EXAFS spectra of Co foil, Co_3O_4, and Co-MFI samples. (c) Local structure of Co-MFI with Co atoms at T_1, T_3, T_7, and T_9 positions by DFT calculations. The distances between the Co atom and the first coordinated O atoms are provided in each image. (d) Charges of Si and Co atoms at the T_3 site and the surrounding O and H atoms. (e) PDOS analysis of the framework O atom surrounding the Si atom (T_3 site of MFI), the framework O atom surrounding the Co atom (T_3 site of Co-MFI), and the Co atom (T_3 site of Co-MFI). The Fermi level is defined at 0 eV. (f) FTIR spectra of Co-MFI were recorded after $CNCD_3$ adsorption and desorption at different temperatures (323, 373, 473, and 573 K). (g) FTIR spectra of Co-MFI were recorded after pyridine adsorption and desorption at different temperatures (473, 573, and 623 K).

MFI framework without Co atoms (Figure 1i) and the MFI framework containing Co atoms at the $T_{1(7)}$ (Figure 1j) and $T_{3(9)}$ sites (Figure 1k). The corresponding STEM-energy dispersive spectroscopy (STEM-EDS) elemental mapping images show that the Co species are ultradispersed within the MFI zeolite matrix (Figures S4 and S5 and Table S2). These results illustrate that Co-MFI possesses a well-defined MFI topology and atomically dispersed Co species embedded into the zeolite framework.

To investigate the coordination environment of Co species in Co-MFI, UV−vis spectroscopic experiments are performed (Figure S6). Three prominent peaks at wavelengths of 653, 582, and 529 nm in the UV−vis spectra, corresponding to $^4A_2 \rightarrow {}^4T_2$, $^4A_2 \rightarrow {}^4T_1$ (^4F), and $^4A_2 \rightarrow {}^4T_1$ (^4P) transitions, respectively, indicate the formation of monomeric tetrahedral Co species in the Co-MFI zeolite.[28,40,41] Furthermore, the structure of Co species in Co-MFI is identified by Co K-edge XAS (Figures 2 and S7). Co_3O_4 and Co foil are used as the references for Co−O−Co and Co−Co bonds. The X-ray absorption near-edge structure (XANES) spectrum of Co-MFI displays two peaks at energies of 7709.8 and 7724.1 eV (Figure 2a). The peak at 7709.8 eV is the pre-edge feature of Co(II), corresponding to the 1s → 3d excitation of Co (low-spin), which is similar to what is observed in Co/SiO_2 with isolated Co(II) atoms.[27,28] The high intensity of the peak at 7724.1 eV in Co-MFI indicates the increased degree of the covalent character of Co(3d)−O(2p). The corresponding Fourier transform (FT) k^3-weighted extended X-ray absorption fine structure (EXAFS) spectrum of Co-MFI presents a noticeable peak at 1.5 Å (Figure 2b), typical for the first shell scattering of O atoms.[27,40] In addition, a small band at 2.7 Å can be detected, which possibly originates from the second shell scattering of Si atoms.[27] The Co K-edge EXAFS spectrum of Co-MFI in k^3-weighted k-space is different from that of Co foil and Co_3O_4 (Figure S7a), suggesting the presence of a unique structure of Co species in Co-MFI. The FT EXAFS spectrum of Co-MFI is fitted by the Artemis software package (Figure S7b and Table S3). The EXAFS spectrum of Co-MFI can be fitted well to the theoretically predicted structure (Figure 2d), indicating that Co-MFI with Co species incorporated into the MFI framework, i.e., $\{(\equiv SiO)_2Co(HO-Si\equiv)_2\}$. These results agree well with the observations by iDPC-STEM and UV−vis spectroscopy, revealing the single tetrahedral Co species being formed and embedded into the corner-sharing network of MFI zeolites in the form of tetrahedral coordination with framework O atoms (Figure 1j,k).

Furthermore, DFT calculations are performed to identify the chemical and electronic structure of Co atoms in MFI zeolites. Co atom incorporation into the siliceous MFI framework causes the special Co species to be embedded into the MFI

https://doi.org/10.1021/jacs.2c02636
J. Am. Chem. Soc. 2022, 144, 12127−12137

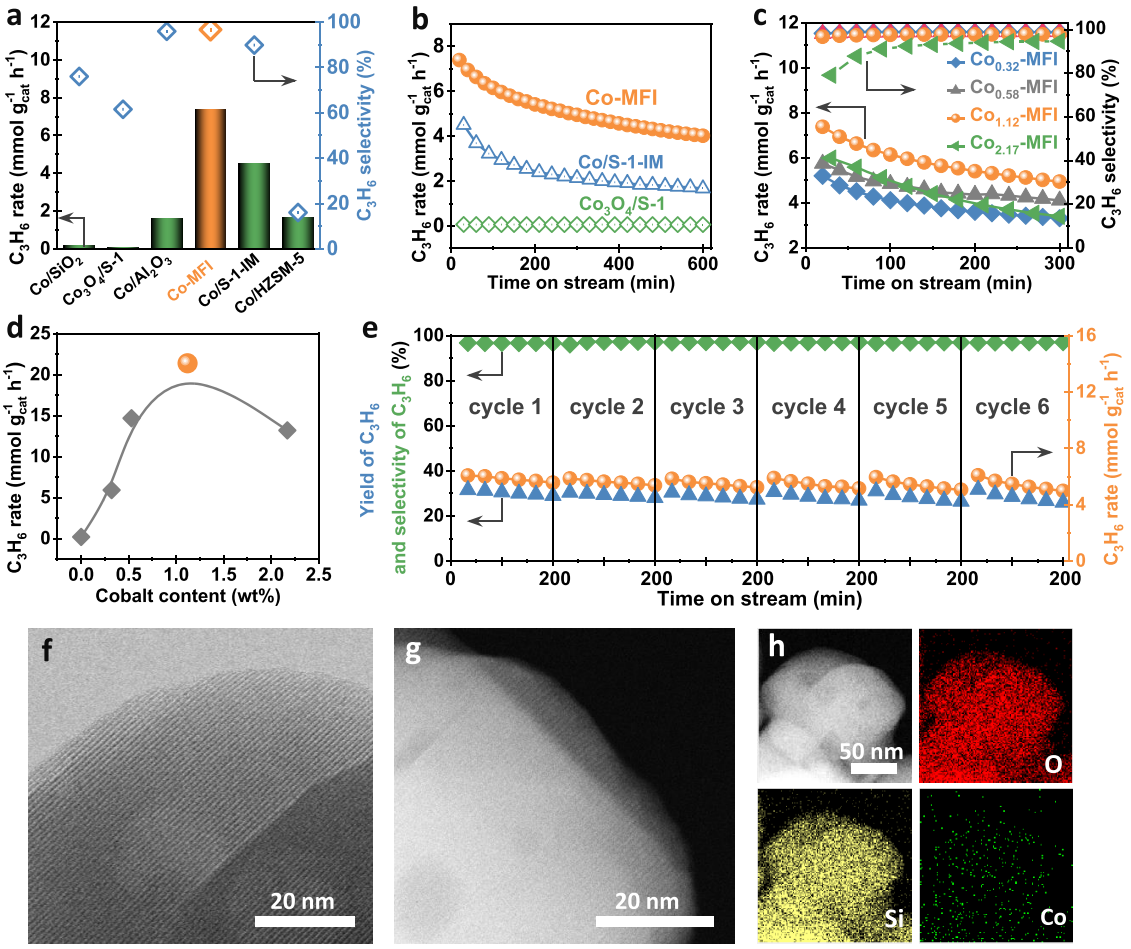

Figure 3. PDH reaction over Co-containing catalysts. (a) Initial C_3H_6 formation rate and selectivity over Co/SiO_2, Co_3O_4/S-1, Co/Al_2O_3, Co-MFI, Co/S-1-IM, and Co/HZSM-5. (b) C_3H_6 formation rates over Co-MFI, Co/S-1-IM, and Co_3O_4/S-1 as a function of time on stream. (c) C_3H_6 formation rates and C_3H_6 selectivity over Co-MFI with different cobalt contents as a function of time on stream. The reaction conditions of (a–c): 0.2 g of catalyst, 580 °C reaction temperature, WHSV = 0.6 h^{-1}, 5 mol % C_3H_8 in Ar. (d) Initial C_3H_6 formation rates over Co-MFI (reaction conditions: 0.05 g of catalyst, 580 °C reaction temperature, WHSV = 2.4 h^{-1}, 5 mol % C_3H_8 in Ar). (e) PDH performance over the Co-MFI catalyst in six reaction-regeneration cycles. Regeneration conditions: 580 °C, air (20 mL/min), 10 min. (f–h) C_s-corrected TEM results of the spent Co-MFI after six cycles: HRTEM (f), HAADF-STEM (g), and STEM-EDS elemental mapping images (h). O (red), Si (yellow), and Co (green).

framework and varies the local environment and electronic states. All the possible locations of Co atoms in the MFI zeolite framework (T_1, T_3, T_7, and T_9) according to the iDPC-STEM characterizations were evaluated theoretically and Co atoms are predicted to be accommodated in the zeolite in a tetrahedral coordination state with two Co−O−Si and two Co···OH−Si linkages, $\{(\equiv SiO)_2Co(HO-Si\equiv)_2\}$ (Figures 2c and S8). The detailed bond length and angle of Co atoms located at different T sites are summarized in Figures 2c and S8. Notably, the two linkages in the tetrahedral coordination state of the Co atom possess two kinds of interactions with the surrounding O atoms, e.g., one is in the form of Co−O−Si with Co−O distances of 1.783 and 1.838 Å and another is in the form of Co···OH−Si with prolonged Co···O distances of 2.084 and 2.932 Å (weak interaction), at the T_3 site. Correspondingly, the electronic states achieved by the charge density analysis show a charge of +1.15 for Co atom, −1.33 and −1.40 for O atoms in Co−O−Si, −1.45 and −1.59 for O atoms in Co···OH−Si, and +0.72 and +0.8 for H atoms in Co···OH−Si (Figure 2d). Comparatively, the charges of Si (T_3 site) and the first coordinated O atoms are +3.17 and −1.59, respectively. PODS analysis conducted for the electronic states of Co-MFI and siliceous MFI zeolites reveals the change of the electronic state brought about by the introduction of Co (Figure 2e). Good symmetry is present in the purely siliceous MFI zeolite without Co, while asymmetric signals can be observed near the Fermi level over the 2p orbitals of the O atom coordinated to the Co atom in Co-MFI, which means that the O atoms are significantly polarized by the Co atom. This is caused by the hybridization between O-2p and Co-3d states, indicating that the introduction of Co atoms into the zeolite framework can significantly affect the electronic and chemical microenvironment of the MFI zeolite and likely lead to the special catalysis of Co-MFI with unique isolated Co-motifs.

To verify the structure of Co-MFI with a $\{(\equiv SiO)_2Co(HO-Si\equiv)_2\}$ local microenvironment, the FTIR experiments were performed for CD_3CN-absorbed Co-MFI and exhibited two bands at 2308 and 2273 cm^{-1} (Figure 2f), which can be attributed to the $\nu(C\equiv N)$ of CD_3CN coordinated to Lewis acid Co sites in $\{(\equiv SiO)_2Co(HO-Si\equiv)_2\}$(2308 cm^{-1}) and silanol sites (Si−OH, 2273 cm^{-1}), respectively.[42−44] Notably, no other characteristic peaks about $\{(\equiv SiO)_2(HO-Si\equiv)Co(OH)\}$ and $\{(\equiv SiO)_2Co(OH)_2\}$ can be observed, suggesting

https://doi.org/10.1021/jacs.2c02636
J. Am. Chem. Soc. 2022, 144, 12127−12137

that almost all Co species are embedded into the MFI framework with a well-defined $\{(\equiv SiO)_2Co(HO-Si\equiv)_2\}$ structure. Since each Co atom is individually embedded into the zeolite framework and bonded with framework oxygen, Co species cannot be reduced to metallic Co by H_2 until temperature increases to 800 °C (Figure S9). The CO-pulse results show that Co-MFI possesses a high Co dispersion of 90.6% (Table S4), suggesting that the Co species are almost atomically dispersed in the MFI zeolite. The acidity of Co-MFI characterized by pyridine adsorption/desorption FTIR spectroscopy also shows that only Lewis acid sites with prominent bands at 1450, 1490, and 1610 cm^{-1} are detected (Figure 2g), indicating that Co embedding into the MFI zeolite framework can only generate the non-Brønsted acidic hydroxyl groups (pyridine adsorption on Brønsted acid sites generally gives rise to the FTIR bands at 1440 and 1550 cm^{-1}, all absent in Figure 2g), which are not capable of protonating pyridine.[45,46] The successful introduction of transition metals, such as Co, into the zeolite resulting in the generation of a pure Lewis acidic environment, would be conducive to the activation of inert alkane molecules, at the same time inhibiting the side reactions of cracking and coke deposition due to no Brønsted acid catalysis.

Based on the above characterizations, the local structure, microenvironment, and electronic states of the Co-MFI zeolite are roundly identified: Single distorted tetrahedral Co species are embedded into the MFI zeolite framework via two strong linkage Co−O−Si and two weak linkages of pseudobridging hydroxyls (Co···OH−Si), named $\{(\equiv SiO)_2Co(HO-Si\equiv)_2\}$. Benefiting from the high dispersion of Co atoms, the delicate tetrahedrally coordinated spatial structure, and the very high specific surface area, the isolated Co-motif combined with the zeolite surrounding creates a more favorable catalytic environment for alkane conversion.

PDH Performance over Co-MFI. Zeolite catalysis relies not only on the local active sites but also on the unique microenvironment characteristic of the crystallized framework and three-dimensional topology. When Co-MFI was successfully synthesized and employed as a catalyst for PDH reaction, atomically dispersed Co atoms and their local MFI structure contributed together to propane activation and transformation, making Co-MFI a very active and selective catalyst compared to other cobalt-supported catalysts (Figures 3 and S10−S14). Typically, Co-MFI exhibits a much higher initial C_3H_6 formation rate and TOF value than that of the other prepared Co-containing catalysts (Figure 3a and Table S4). The ligand-protected hydrothermal synthesis approach can construct the isolated active center of $\{(\equiv SiO)_2Co(HO-Si\equiv)_2\}$ with tetrahedrally coordinated Co species in Co-MFI, which presents high efficiency and selectivity in the PDH reaction. Figure 3b depicts the stability tests of the Co-MFI zeolite during the PDH reaction and a high C_3H_6 formation rate is kept during the 600 min time on stream. In contrast, Co/S-1-IM, prepared by the wet impregnation method for Co species introduction on purely siliceous MFI zeolite, exhibits lower PDH performance than Co-MFI. Usually, metallic species supported on zeolites, prepared by the wet impregnation method, possessed complex metallic species, e.g., isolated metallic sites,[47] ultrasmall metallic clusters,[48,49] and bulk metallic oxides.[50−52] Herein, both tetrahedral Co species, CoO_x clusters and nanoparticles are formed on Co/S-1-IM, as demonstrated by CD_3CN-FTIR (Figure S15), TEM (Figure S16), and UV−vis spectra (Figure S17). When Co_3O_4 was introduced onto the S-1 zeolite by mechanically mixing Co_3O_4 and S-1, Co_3O_4/S-1 is composed of nanoparticle Co species and the S-1 zeolite (Figure S18) and displays almost no catalytic performance for propane conversion. The different ways of introducing Co into S-1 bring about the difference in the combination of Co species and zeolites (Figure S19). Integration of Co species with the zeolite via embedding Co species into the MFI framework to form tetrahedrally coordinated Co species is the key to achieving the high-efficient PDH performance. The siliceous MFI structure accommodates the reaction center of $\{(\equiv SiO)_2Co(HO-Si\equiv)_2\}$ and works together with these uniform and highly dispersed single Co species in the PDH reaction.

Figure 3c shows the C_3H_6 formation rates of Co-MFI with different Co contents from 0.32 to 2.17 wt % as a function of time on stream. At Co contents lower than 1.12 wt %, the C_3H_6 formation rates of Co-MFI increase with the Co contents. With further increasing the Co content up to 2.17 wt %, the activity and selectivity of the PDH reaction over Co-MFI decrease. A volcano type variation tendency in the initial C_3H_6 formation rate is presented in Figure 3d with Co content variation. In terms of the above characterizations, all Co species are embedded into the MFI zeolite framework at low Co content of 0.32−1.12 wt %, corresponding to the PDH conversion increases over Co-MFI with the intensification of the active center, $\{(\equiv SiO)_2Co(HO-Si\equiv)_2\}$. However, with much more Co atom incorporation with Co content up to 2.17 wt %, with the appearance of CoO_x clusters or nanoparticles, the conversion rate of PDH reaction declines. This confirms that isolated Co species with the tetrahedrally coordinated state in the MFI zeolite framework are of extremely high reactivity for the PDH reaction, much higher than CoO_x clusters or nanoparticles (Figure S20). The TOF values of the previous Co-, Cr-, and Pt-based catalysts are calculated and listed in Tables S5−S7. Notably, Co-MFI exhibits a high TOF of 124.3 h^{-1}, which is comparable to that of some Pt-based catalysts and much higher than that of previously reported Co- and Cr-based catalysts, illustrating the excellent PDH performance of Co-MFI. The cycle stability test demonstrates the high cycle stability of the Co-MFI catalyst (Figure 3e). An initial C_3H_6 formation rate of 5.05 mmol g_{cat}^{-1} h^{-1} accompanied by 96.7% C_3H_6 selectivity is presented in the first cycle, and these two values are well maintained after six cycles, with a C_3H_6 formation rate of 5.07 mmol g_{cat}^{-1} h^{-1} and 96.8% C_3H_6 selectivity.

The C_s-corrected TEM characterization of the spent Co-MFI zeolite (Figure 3f−h) after the sixth reaction-regeneration cycle shows the same micromorphology as that of the fresh Co-MFI zeolite (Figure 1). The STEM-EDS mapping images also reveal the homogeneous distribution of Co species in the spent Co-MFI (Figure 3h). Multitechniques employed for the measurement of the spent Co-MFI after regeneration in an air atmosphere and reduction in H_2 flow (Figures S21−S27) illustrate the good maintenance of the structure of the Co center, $\{(\equiv SiO)_2Co(HO-Si\equiv)_2\}$, and the MFI framework during the long-term and recycling PDH reaction. The MFI zeolite framework provides an extremely unique microenvironment for accommodating and stabilizing the isolated Co species under PDH conditions.

To better understand the superior PDH performance of the Co-MFI zeolite, C_3H_8-TPSR experiments were performed over Co-MFI in a stable C_3H_8 flow (Figure S28). The H_2 and C_3H_6 signals increase predominantly, while signals from CH_4, C_2H_4,

https://doi.org/10.1021/jacs.2c02636
J. Am. Chem. Soc. 2022, 144, 12127−12137

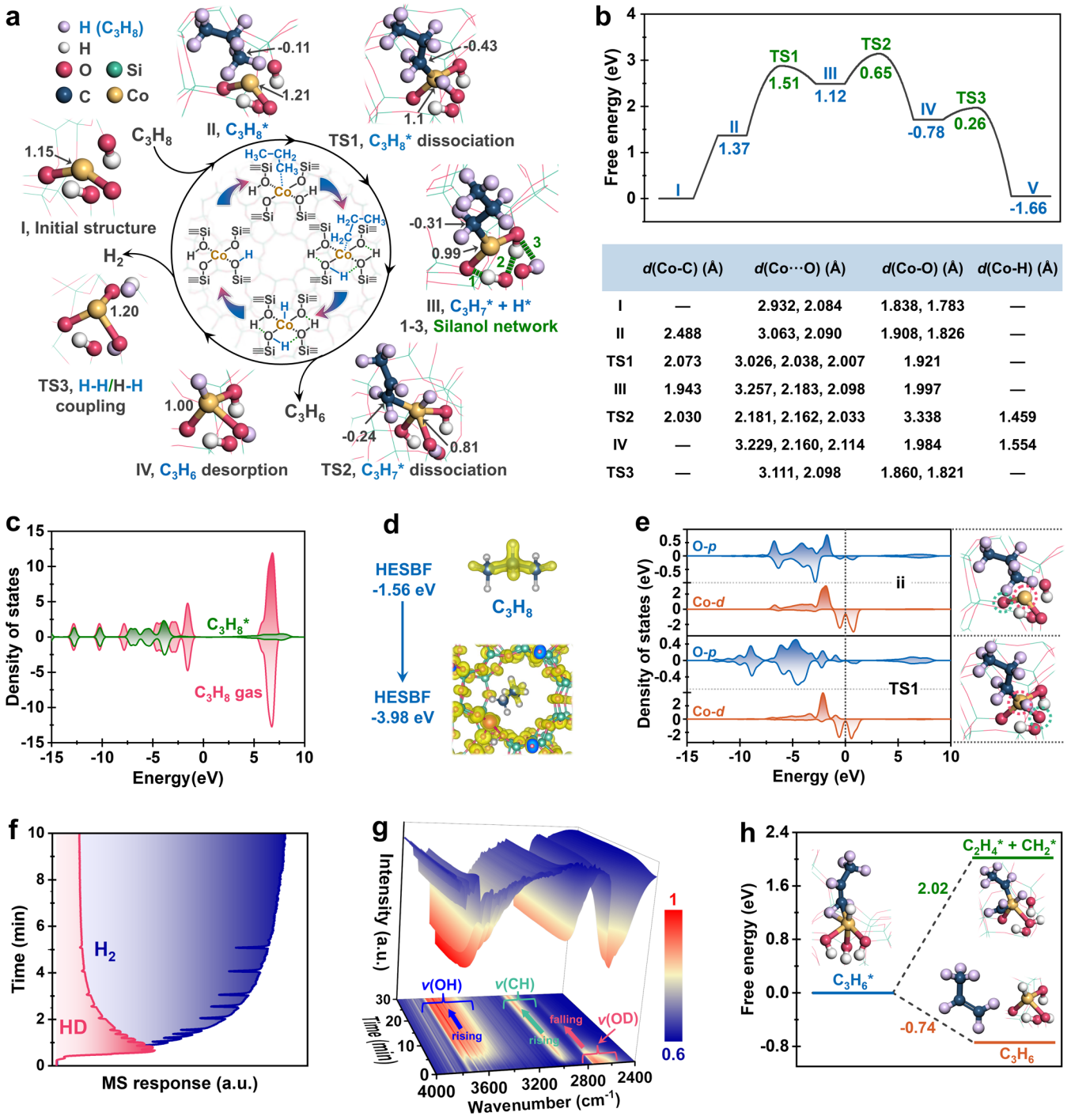

	d(Co-C) (Å)	d(Co···O) (Å)	d(Co-O) (Å)	d(Co-H) (Å)
I	—	2.932, 2.084	1.838, 1.783	—
II	2.488	3.063, 2.090	1.908, 1.826	—
TS1	2.073	3.026, 2.038, 2.007	1.921	—
III	1.943	3.257, 2.183, 2.098	1.997	—
TS2	2.030	2.181, 2.162, 2.033	3.338	1.459
IV	—	3.229, 2.160, 2.114	1.984	1.554
TS3	—	3.111, 2.098	1.860, 1.821	—

Figure 4. Mechanism investigation of the PDH reaction on the Co-MFI zeolite. (a) Proposed catalytic cycle of the PDH reaction over the Co-MFI zeolite (Co atoms at the T_3 site). Optimized structures, transition states, and the charge of the Co atom are given. The charge of Co and C atoms and the silanol network with three hydrogen bonds (III, 1−3) are highlighted. (b) Energy profile of the PDH reaction over the Co-MFI zeolite following the reaction route in (a), and DFT predicted the Co−C, Co−O, and Co−H distance. Blue and green represent the ΔG and barrier, respectively. (c) PDOS analysis for C_3H_8 inside and outside of the Co-MFI zeolite. (d) Charge density of the HESBF for C_3H_8 inside and outside of the Co-MFI zeolite. (e) PDOS analysis for Co and surrounding O atoms at the initial stage of II and TS1. The Fermi level is defined to 0 eV. (f) Online MS analysis of the generated H−D and H_2 in the PDH reaction over D-labeled Co-MFI. (g) In situ FTIR spectroscopy study of the D-labeled Co-MFI during the PDH reaction. (h) Energy profile of C_3H_6* cracking and desorption over Co-MFI with Co atoms located at the T_3 site.

and C_2H_6 are detected in very low intensity even at 600 °C, indicating the highly reactive and selective PDH reaction over Co-MFI. Comparatively, C_3H_8-TPSR over the supported catalyst, Co/HZSM-5 and Co/SiO_2, shows much more byproduct generation, such as CH_4, C_2H_4, and C_2H_6. The catalysis of Co-MFI not only guarantees the highly active PDH reaction due to the performance of highly isolated Lewis acidic sites of $\{(\equiv SiO)_2Co(HO-Si\equiv)_2\}$ in the catalyst but also ensures the selective generation of the target product by decreasing the possible side reactions, such as catalytic cracking and coke deposition by the construction of non-Brønsted acidic zeolite catalysts. During the PDH reaction, the

https://doi.org/10.1021/jacs.2c02636
J. Am. Chem. Soc. 2022, 144, 12127−12137

quick leaving of the generated C_3H_6 from Co-MFI is confirmed by the C_3H_6 adsorption−desorption experiments (Figures S29−S31). Typically, the formation of coke precursors stems from the deep dehydrogenation of C_3H_6, going through the reaction route from propenyl species to propyne. Also, cracking or aromatization is likely to occur for the strongly adsorbed C_3H_6. Over Co-MFI, weak interaction with the generated C_3H_6 inhibits the further transformation of the generated product and achieves nearly 100% C_3H_6 selectivity.

Mechanism Investigation of the PDH Reaction over Co-MFI. The above characterizations and catalytic results demonstrate that the isolated tetrahedral Co sites are embedded into the zeolite framework to form the Co-MFI zeolite. The Co-motif in the form of $\{(\equiv SiO)_2Co(HO-Si\equiv)_2\}$ and the surrounding zeolite microenvironment work synergistically for the highly efficient PDH performance. To understand the reaction mechanism, DFT calculations of C_3H_8 activation were performed over Co-MFI with framework Si atoms replaced by Co atoms at the observed sites (T_1, T_3, T_7, and T_9, Figure 1) and a referenced site (T_{10}) according to the MFI topology. Since C_3H_8* (in the adsorption state) dissociation has been confirmed as the rate-determining step in the PDH process in the previous studies,[53−56] the energy profiles of C_3H_8* → C_3H_7* + H* on these sites are studied (Figures S32−S36 and Table S8). Among all the T sites, the C−H bond dissociation at the T_3 site is the most energetically favorable with a kinetic barrier of 1.51 eV and a reaction free energy of 1.12 eV. The preference in kinetics and thermodynamics at the T_3 site can be attributed to its unique microenvironment, where the produced C_3H_7* intermediate encounters very weak steric hindrance effects from the zeolite framework. In the following, we will only discuss the reaction mechanism and electronic origins over Co-MFI with Co atoms embedded at the T_3 site.

A possible reaction pathway and free energies of the PDH reaction on Co-MFI are depicted in Figure 4a−e. Once the gas-phase C_3H_8 molecule is adsorbed on the reaction center of $\{(\equiv SiO)_2Co(HO-Si\equiv)_2\}$ in Co-MFI (I in Figure 4a), preactivation of C_3H_8 would occur at this moment (II in Figure 4a). The analysis of PDOS (Figure 4c) and the highest electronic states below the Fermi level (HESBF, Figure 4d) compares the C_3H_8 inside and outside of the Co-MFI zeolite confined space. The LUMO of C_3H_8, which is assigned to p states of carbon atoms, shifts downward, as C_3H_8 is placed from the gas phase to a confined state, which means the adsorbed C_3H_8* can accept electrons easily than a molecule in the gas phase. In other words, the adsorbed C_3H_8* has been preactivated by Co-MFI. Furthermore, the Bader charge analysis shows that the carbon atom in the methyl of C_3H_8 indeed accepts electrons (−0.11 e) in the first C−H bond dissociation step. These electronic factors discussed above strongly indicate the existence of the preactivation effect for C_3H_8, as being confined within the unique microenvironment of the Co-MFI zeolite. The embedded Co atom and its surrounding microenvironment collectively provide the preactivation.

After the preactivation, the C_3H_8* species can be dissociated into C_3H_7* and H* on the active site of $\{(\equiv SiO)_2Co(HO-Si\equiv)_2\}$ (III in Figure 4a). As the neighboring O atoms are significantly polarized by the Co atom, as shown in Figure 2f, therefore, the H* prefers to bond with the O atom after C_3H_8* dissociation, resulting in a stable $\{(\equiv SiO)(C_3H_7)Co(HO-Si\equiv)_3\}$ intermediate (IV in Figure 4a). Figures 4e and S37 show that the electronic states of O and H atoms are stabilized at a more negative energy level, which means the tight bonding between O and H atoms. Simultaneously, a strong Co-C_3H_7* bond can be formed after the first dissociation step. With the aid of distorted tetrahedral Co sites and polarized O atoms in the reaction center of $\{(\equiv SiO)_2Co(HO-Si\equiv)_2\}$, the first C−H bond dissociation can be realized by overcoming an energy barrier of 1.51 eV. After the first C−H bond dissociation, the silanol network with three hydrogen bonds can be formed among these pseudobridging hydroxyls. Then, the adsorbed C_3H_7* intermediate is dissociated into C_3H_6* and H* with a low barrier of 0.65 eV (ΔG = −0.78 eV), resulting in a Co−H bond. Subsequently, a C_3H_6 molecule can be released and an intermediate in the form of $\{(\equiv SiO)CoH^{\delta-}(H^{\delta+}O-Si\equiv)_3\}$ will be formed(IV). Note that at this moment, the H atom attached to the Co atom is negatively charged, while the H atom in the hydroxyl group is positively charged. At last, the coupling reaction between $H^{\delta-}$ and $H^{\delta+}$ in$\{(\equiv SiO)-CoH^{\delta-}(H^{\delta+}O-Si\equiv)_3\}$ produces a H_2 molecule with a low barrier of 0.26 eV (ΔG = −1.66 eV). The active site of Co-MFI participates in all the steps, including adsorption, activation, dissociation of propane, stabilization and acquisition of C_3H_7* and H*, and release of H_2. With the completion of the entire catalytic cycle, the reaction center turns to the initial structure, $\{(\equiv SiO)_2Co(HO-Si\equiv)_2\}$, and is ready for the next and repetitive catalytic cycle for the PDH reaction.

Bader charge analysis reveals that the Co reaction center is unique and acts as an electron reservoir, where the charge of the Co atom is dynamically evolved in the whole catalytic process (Figure 4a). After the first C−H bond dissociation, three hydroxyl groups are formed. The positive charge of the Co site decreases gradually from +1.21 (II), +1.10 (TS1) to +0.99 (III). Meanwhile, the surrounding oxygen atoms can bond with the dissociated H* and result in three pseudobridging hydroxyls with positively charged H atoms (Figure S38). Then, C_3H_7* is dissociated into C_3H_6* and H* with the dynamical change of the Co charge from +0.81 (TS2) to +1.00(IV), resulting in a Co−H bond. H−H coupling enhances the positive charge on the Co atom (+1.20, TS3) and then the electronic state of the Co reaction center restores to the initial state (+1.15, I). It is noticeable that the O atom acts as a bridge for electron transfer because of the 3d−2p orbital hybridization (Figure 4e), promoting the PDH catalytic cycle.

To confirm the proposed mechanism, deuterium-labeling experiments were performed over Co-MFI before the catalytic test (Figure S39). The H atoms in the Co-motif $\{(\equiv SiO)_2Co(HO-Si\equiv)_2\}$ of Co-MFI can be exchanged by D atoms to form OD groups in the D_2 atmosphere at a temperature of 580 °C, evidenced by the in situ FTIR spectroscopy with the emergence of new absorbance bands from OD in the region of 2500−2800 cm^{-1}. Then, the deuterium-labeled Co-MFI was tested for C_3H_8 conversion. The online mass spectrometry (MS) results demonstrate the formation of HD molecules at the initial stage of the PDH reaction (Figure 4f). At the same time, in situ FTIR measurement detects that the OD absorbance band at 2500−2800 cm^{-1} progressively declines and finally disappears with continuous C_3H_8 feeding (Figure 4g), and at the same time, the OH bonds (3400−3700 cm^{-1}) on the surface are restored. Comparatively, for the PDH reaction performed over D-labeled S-1, the formation rates of HD and H_2 are both much lower than that over D-labeled Co-MFI. Also, the slow

https://doi.org/10.1021/jacs.2c02636
J. Am. Chem. Soc. 2022, 144, 12127−12137

H-D exchange between D_2 and surface hydroxyls in Co-MFI at the same temperature was evidenced experimentally and theoretically (Figures S40−S42). Especially, the appearance of HD was ahead of H_2 over Co-MFI at the very beginning of the PDH reaction (Figure S40). Therefore, HD formation over D-labeled Co-MFI was confirmed to be mainly from the participation of hydroxyl groups of Co-MFI in the dehydrogenation procedure as suggested in Figure 4a. All these indicate that the cooperation of Co species and the hydroxyl groups in the neighborhood in Co-MFI contributes to the efficient PDH reaction.

The PDH reaction over the Co-MFI zeolite exhibits extremely high C_3H_6 selectivity, which benefits from the quick leaving of the generated C_3H_6 from Co-MFI, as presented in the C_3H_6 adsorption−desorption experiments (Figures S29−S31). After PDH over Co-MFI, in addition to C_3H_6 release from the catalyst surface, some secondary reaction routes from the precursor of C_3H_6 were also evaluated theoretically. The C_3H_6* cracking process is endothermic with a ΔG of 2.02 eV (Figure 4h). The dehydrogenation of C_3H_6* (C_3H_6* → C_3H_5* + H*) is also endothermic with a ΔG of 0.68 eV (Figure S43). Comparatively, the release of C_3H_6 from its precursor species is exothermic with a ΔG of −0.74 eV. Since the generated C_3H_6 can be easily desorbed from the Co sites during the PDH reaction, at the same time cracking and deep dehydrogenation of propene are both thermodynamically unfavorable, highly selective PDH reaction can be realized. In summary, we reveal the underlined nature of why Co-MFI exhibits efficient and selective catalysis in the PDH process: The Co species embedded into the zeolite framework, polarized oxygen atoms in the surrounding, and the spatial microenvironment of the zeolite can collectively participate in and promote the PDH process, which is like enzyme catalysis.

CONCLUSIONS

In this work, we present direct evidence for the construction of isolated Co-motifs within the purely siliceous MFI zeolite framework. The location, uniformity, and exact structure of Co-MFI are fully identified by iDPC-STEM, XAS, pyridine/CD_3CN FT-IR, and UV−vis spectroscopy, revealing that the isolated Co-motifs with the distorted tetrahedral structure of $\{(\equiv SiO)_2Co(HO-Si\equiv)_2\}$ are homogeneously embedded into the $T_{1(7)}$ and $T_{3(9)}$ sites of MFI zeolites. These isolated Co-motif species in the MFI zeolite framework as well-defined active sites together with the unique zeolite microenvironment commit to highly efficient PDH performance.

Like enzymatic catalysis, the participation of Co-motifs in the PDH reaction as the reaction center is in a special dynamically cooperative mode. First, Co-MFI catalyzes C−H bond dissociation of C_3H_8 in which the Co-motif center simultaneously accepts C_3H_7* and H* atoms and evolves itself to the intermediate state of $\{(\equiv SiO)(C_3H_7)Co(HO-Si\equiv)_3\}$. After this, the second C−H dissociation from C_3H_7* is accompanied by the Co-motif self-evolution to another intermediate state of $\{(\equiv SiO)CoH^{\delta-}(H^{\delta+}O-Si\equiv)_3\}$ for accepting another H*. Finally, the leaving of C_3H_6 and H_2 from this complex restored the Co-motif to its initial state of $\{(\equiv SiO)_2Co(HO-Si\equiv)_2\}$.

The catalytic mode with the direct participation of Co-MFI in the PDH reaction involves the dynamic and continuous evolution of the entity of the Co-motif reaction center, not only being varied in electronic states but also in the coordination states. These dynamic evolutions and restoration of the Co-motif reaction center proceed in a continuous and repetitive way to meet the requirements from the series of elementary steps in the PDH catalytic cycle, including propane adsorption, activation, C−H bond dissociation, and dehydrogenation. The proposed pathway with the cross-talk of the Co-motif center and the reactant is supported by in situ FTIR spectroscopy and online mass spectroscopy by tracking the hydroxyl group evolution and hydrogen generation with the employment of the deuterium-labeling technique.

ASSOCIATED CONTENT

Supporting Information

The Supporting Information is available free of charge at https://pubs.acs.org/doi/10.1021/jacs.2c02636.

The experiments, characterization results (XRD, HAADF-STEM, UV−vis, CD_3CN-FTIR, in situ AP-XPS, TPD-MS), DFT calculations, and other supplementary results and discussion of reaction and spectroscopy (PDF)

AUTHOR INFORMATION

Corresponding Authors

Jianping Xiao − *State Key Laboratory of Catalysis, Dalian Institute of Chemical Physics, Chinese Academy of Sciences, Dalian 116023, People's Republic of China; Dalian National Laboratory for Clean Energy, Dalian Institute of Chemical Physics, Chinese Academy of Sciences, Dalian 116023, People's Republic of China; University of Chinese Academy of Sciences, Beijing 100049, People's Republic of China;* orcid.org/0000-0003-1779-6140; Email: xiao@dicp.ac.cn

Yingxu Wei − *National Engineering Research Center of Lower-Carbon Catalysis Technology, Dalian National Laboratory for Clean Energy, iChEM (Collaborative Innovation Center of Chemistry for Energy Materials), Dalian Institute of Chemical Physics, Chinese Academy of Sciences, Dalian 116023, People's Republic of China;* orcid.org/0000-0002-0412-1980; Email: weiyx@dicp.ac.cn

Zhongmin Liu − *National Engineering Research Center of Lower-Carbon Catalysis Technology, Dalian National Laboratory for Clean Energy, iChEM (Collaborative Innovation Center of Chemistry for Energy Materials) and State Key Laboratory of Catalysis, Dalian Institute of Chemical Physics, Chinese Academy of Sciences, Dalian 116023, People's Republic of China; University of Chinese Academy of Sciences, Beijing 100049, People's Republic of China;* orcid.org/0000-0002-7999-2940; Email: liuzm@dicp.ac.cn

Authors

Zhong-Pan Hu − *National Engineering Research Center of Lower-Carbon Catalysis Technology, Dalian National Laboratory for Clean Energy, iChEM (Collaborative Innovation Center of Chemistry for Energy Materials), Dalian Institute of Chemical Physics, Chinese Academy of Sciences, Dalian 116023, People's Republic of China*

Gangqiang Qin − *State Key Laboratory of Catalysis, Dalian Institute of Chemical Physics, Chinese Academy of Sciences, Dalian 116023, People's Republic of China; University of Chinese Academy of Sciences, Beijing 100049, People's Republic of China*

https://doi.org/10.1021/jacs.2c02636
J. Am. Chem. Soc. 2022, 144, 12127−12137

Jingfeng Han − *National Engineering Research Center of Lower-Carbon Catalysis Technology, Dalian National Laboratory for Clean Energy, iChEM (Collaborative Innovation Center of Chemistry for Energy Materials), Dalian Institute of Chemical Physics, Chinese Academy of Sciences, Dalian 116023, People's Republic of China*

Wenna Zhang − *National Engineering Research Center of Lower-Carbon Catalysis Technology, Dalian National Laboratory for Clean Energy, iChEM (Collaborative Innovation Center of Chemistry for Energy Materials), Dalian Institute of Chemical Physics, Chinese Academy of Sciences, Dalian 116023, People's Republic of China*

Nan Wang − *National Engineering Research Center of Lower-Carbon Catalysis Technology, Dalian National Laboratory for Clean Energy, iChEM (Collaborative Innovation Center of Chemistry for Energy Materials), Dalian Institute of Chemical Physics, Chinese Academy of Sciences, Dalian 116023, People's Republic of China; University of Chinese Academy of Sciences, Beijing 100049, People's Republic of China*

Yijun Zheng − *National Engineering Research Center of Lower-Carbon Catalysis Technology, Dalian National Laboratory for Clean Energy, iChEM (Collaborative Innovation Center of Chemistry for Energy Materials), Dalian Institute of Chemical Physics, Chinese Academy of Sciences, Dalian 116023, People's Republic of China*

Qike Jiang − *Dalian National Laboratory for Clean Energy, Dalian Institute of Chemical Physics, Chinese Academy of Sciences, Dalian 116023, People's Republic of China*

Te Ji − *SSRF, Shanghai Institute of Applied Physics, Chinese Academy of Sciences, Shanghai 201800, People's Republic of China*

Zhong-Yong Yuan − *Key Laboratory of Advanced Energy Materials Chemistry (Ministry of Education), School of Materials Science and Engineering, Nankai University, Tianjin 300350, People's Republic of China;* orcid.org/0000-0002-3790-8181

Complete contact information is available at: https://pubs.acs.org/10.1021/jacs.2c02636

Author Contributions

[▽]Z.P.H. and G.Q. contributed equally.

Notes

The authors declare no competing financial interest.
[○]Lead contact.

■ ACKNOWLEDGMENTS

The authors are thankful for the financial support from the National Natural Science Foundation of China (No. 21991092, 21991090, and 51701201), the Key Research Program of Frontier Sciences, CAS, Grant No. QYZDY-SSW-JSC024, the International Partnership Program of Chinese Academy of Sciences (121421KYSB20180007), Dalian Institute of Chemical Physics, Grant No. DICP I201926, the China Postdoctoral Science Foundation (2019M661147), the Excellent Postdoctoral Support Program of Dalian Institute of Chemical Physics, CAS, the Excellent Research Assistant Funding Project of CAS, and the DNL Cooperation Fund, CAS (DNL201903). J.X. thanks the National Key Research and Development Program of China (No. 2021YFA1500702), the National Natural Science Foundation of China (No. 22172156 and 91945302), the DNL Cooperation Fund, CAS (DNL202003), LiaoNing Revitalization Talents Program (No. XLYC1907099), and Strategic Priority Research Program of the Chinese Academy of Sciences (No. XDB36030200). The authors thank BSRF and SSRF (BL06B) beamline for experimental data collection and M. Li (Department of Industrial Chemistry "Toso Montanari," University of Bologna, Viale del Risorgimento 4, Bologna 40136, Italy) and X. Liu (CAS Key Laboratory of Science and Technology on Applied Catalysis, Dalian Institute of Chemical Physics, Chinese Academy of Sciences, Dalian 116023, People's Republic of China) for XAS analysis.

■ REFERENCES

(1) Liu, L.; Lopez-Haro, M.; Lopes, C. W.; Li, C.; Concepcion, P.; Simonelli, L.; Calvino, J. J.; Corma, A. Regioselective Generation and Reactivity Control of Subnanometric Platinum Clusters in Zeolites for High-Temperature Catalysis. *Nat. Mater.* **2019**, *18*, 866−873.

(2) Ryoo, R.; Kim, J.; Jo, C.; Han, S. W.; Kim, J. C.; Park, H.; Han, J.; Shin, H. S.; Shin, J. W. Rare-Earth−Platinum Alloy Nanoparticles in Mesoporous Zeolite for Catalysis. *Nature* **2020**, *585*, 221−224.

(3) Chai, Y.; Wu, G.; Liu, X.; Ren, Y.; Dai, W.; Wang, C.; Xie, Z.; Guan, N.; Li, L. Acetylene-Selective Hydrogenation Catalyzed by Cationic Nickel Confined in Zeolite. *J. Am. Chem. Soc.* **2019**, *141*, 9920−9927.

(4) Zhong, J.; Xu, Y.; Liu, Z. Heterogeneous Non-mercury Catalysts for Acetylene Hydrochlorination: Progress, Challenges, and Opportunities. *Green Chem.* **2018**, *20*, 2412−2427.

(5) Gordon, C. P.; Engler, H.; Tragl, A. S.; Plodinec, M.; Lunkenbein, T.; Berkessel, A.; Teles, J. H.; Parvulescu, A. N.; Copéret, C. Efficient Epoxidation over Dinuclear Sites in Titanium Silicalite-1. *Nature* **2020**, *586*, 708−713.

(6) Lin, M.; Xia, C.; Zhu, B.; Li, H.; Shu, X. Green and Efficient Epoxidation of Propylene with Hydrogen Peroxide (HPPO Process) Catalyzed by Hollow TS-1 Zeolite: A 1.0 kt/a Pilot-Scale Study. *Chem. Eng. J.* **2016**, *295*, 370−375.

(7) Lin, S.; Zhi, Y.; Chen, W.; Li, H.; Zhang, W.; Lou, C.; Wu, X.; Zeng, S.; Xu, S.; Xiao, J.; Zheng, A.; Wei, Y.; Liu, Z. Molecular Routes of Dynamic Autocatalysis for Methanol-to-Hydrocarbons Reaction. *J. Am. Chem. Soc.* **2021**, *143*, 12038−12052.

(8) Wu, X.; Xu, S.; Zhang, W.; Huang, J.; Li, J.; Yu, B.; Wei, Y.; Liu, Z. Direct Mechanism of the First Carbon−Carbon Bond Formation in the Methanol-to-Hydrocarbons Process. *Angew. Chem., Int. Ed.* **2017**, *56*, 9039−9043.

(9) Zhang, W.; Chen, J.; Xu, S.; Chu, Y.; Wei, Y.; Zhi, Y.; Huang, J.; Zheng, A.; Wu, X.; Meng, X.; Xiao, F.; Deng, F.; Liu, Z. Methanol to Olefins Reaction over Cavity-Type Zeolite: Cavity Controls the Critical Intermediates and Product Selectivity. *ACS Catal.* **2018**, *8*, 10950−10963.

(10) Li, C.; Ferri, P.; Paris, C.; Moliner, M.; Boronat, M.; Corma, A. Design and Synthesis of the Active Site Environment in Zeolite Catalysts for Selectively Manipulating Mechanistic Pathways. *J. Am. Chem. Soc.* **2021**, *143*, 10718−10726.

(11) Slater, A. G.; Cooper, A. I. Porous materials. Function-Led Design of New Porous Materials. *Science* **2015**, *348*, No. aaa8075.

(12) Liu, L.; Corma, A. Isolated Metal Atoms and Clusters for Alkane Activation: Translating Knowledge from Enzymatic and Homogeneous to Heterogeneous Systems. *Chem* **2021**, *7*, 2347−2384.

(13) Sushkevich, V. L.; Palagin, D.; Ranocchiari, M.; van Bokhoven, J. A. Selective Anaerobic Oxidation of Methane Enables Direct Synthesis of Methanol. *Science* **2017**, *356*, 523−527.

(14) Snyder, B. E.; Vanelderen, P.; Bols, M. L.; Hallaert, S. D.; Böttger, L. H.; Ungur, L.; Pierloot, K.; Schoonheydt, R. A.; Sels, B. F.; Solomon, E. I. The Active Site of Low-temperature Methane Hydroxylation in Iron-containing Zeolites. *Nature* **2016**, *536*, 317−321.

(15) Snyder, B. E. R.; Bols, M. L.; Rhoda, H. M.; Plessers, D.; Schoonheydt, R. A.; Sels, B. F.; Solomon, E. I. Cage Effects Control

the Mechanism of Methane Hydroxylation in Zeolites. *Science* **2021**, *373*, 327−331.
(16) Scott, S. Bioinspired Methane Oxidation in a Zeolite. *Science* **2021**, *373*, 277−278.
(17) Hu, Z. P.; Han, J.; Wei, Y.; Liu, Z. Dynamic Evolution of Zeolite Framework and Metal-Zeolite Interface. *ACS Catal.* **2022**, *12*, 5060−5076.
(18) Paolucci, C.; Khurana, I.; Parekh, A. A.; Li, S.; Shih, A. J.; Li, H.; Di Iorio, J. R.; Albarracin-Caballero, J. D.; Yezerets, A.; Miller, J. T.; Delgass, W. N.; Ribeiro, F. H.; Schneider, W. F.; Gounder, R. Dynamic Multinuclear Sites Formed by Mobilized Copper Ions in NO_x Selective Catalytic Reduction. *Science* **2017**, *357*, 898−903.
(19) Shan, J.; Li, M.; Allard, L. F.; Lee, S.; Flytzani-Stephanopoulos, M. Mild Oxidation of Methane to Methanol or Acetic Acid on Supported Isolated Rhodium Catalysts. *Nature* **2017**, *551*, 605−608.
(20) Zhao, D.; Tian, X.; Doronkin, D. E.; Han, S.; Kondratenko, V. A.; Grunwaldt, J. D.; Perechodjuk, A.; Vuong, T. H.; Rabeah, J.; Eckelt, R.; Rodemerck, U.; Linke, D.; Jiang, G.; Jiao, H.; Kondratenko, E. V. In situ Formation of ZnO_x Species for Efficient Propane Dehydrogenation. *Nature* **2021**, *599*, 234−238.
(21) Wang, Y.; Hu, Z. P.; Lv, X.; Chen, L.; Yuan, Z. Y. Ultrasmall PtZn Bimetallic Nanoclusters Encapsulated in Silicalite-1 Zeolite with Superior Performance for Propane Dehydrogenation. *J. Catal.* **2020**, *385*, 61−69.
(22) Yang, Z.; Li, H.; Zhou, H.; Wang, L.; Wang, L.; Zhu, Q.; Xiao, J.; Meng, X.; Chen, J.; Xiao, F. S. Coking-Resistant Iron Catalyst in Ethane Dehydrogenation Achieved through Siliceous Zeolite Modulation. *J. Am. Chem. Soc.* **2020**, *142*, 16429−16436.
(23) Corma, A.; Nemeth, L. Z.; Renz, M.; Valencia, S. Sn-Zeolite Beta as a Heterogeneous Chemoselective Catalyst for Baeyer-Villiger Oxidations. *Nature* **2001**, *412*, 423−425.
(24) Ferrini, P.; Dijkmans, J.; De Clercq, R.; Van de Vyver, S.; Dusselier, M.; Jacobs, P. A.; Sels, B. F. Lewis Acid Catalysis on Single Site Sn Centers Incorporated into Silica Hosts. *Coord. Chem. Rev.* **2017**, *343*, 220−255.
(25) Wang, N.; Sun, Q.; Yu, J. Ultrasmall Metal Nanoparticles Confined within Crystalline Nanoporous Materials: A Fascinating Class of Nanocatalysts. *Adv. Mater.* **2019**, *31*, No. e1803966.
(26) Wang, L.; Wang, L.; Meng, X.; Xiao, F. S. New Strategies for the Preparation of Sinter-Resistant Metal-Nanoparticle-Based Catalysts. *Adv. Mater.* **2019**, *31*, No. e1901905.
(27) Hu, B.; "Bean" Getsoian, A.; Schweitzer, N. M.; Das, U.; Kim, H.; Niklas, J.; Poluektov, O.; Curtiss, L. A.; Stair, P. C.; Miller, J. T.; Hock, A. S. Selective Propane Dehydrogenation with Single-Site Co^{II} on SiO_2 by a Non-redox Mechanism. *J. Catal.* **2015**, *322*, 24−37.
(28) Estes, D. P.; Siddiqi, G.; Allouche, F.; Kovtunov, K. V.; Safonova, O. V.; Trigub, A. L.; Koptyug, I. V.; Copéret, C. C-H Activation on Co,O Sites: Isolated Surface Sites versus Molecular Analogs. *J. Am. Chem. Soc.* **2016**, *138*, 14987−14997.
(29) Dai, Y.; Gu, J.; Tian, S.; Wu, Y.; Chen, J.; Li, F.; Du, Y.; Peng, L.; Ding, W.; Yang, Y. γ-Al_2O_3 Sheet-Stabilized Isolate Co^{2+} for Catalytic Propane Dehydrogenation. *J. Catal.* **2020**, *381*, 482−492.
(30) Dai, Y.; Wu, Y.; Dai, H.; Gao, X.; Tian, S.; Gu, J.; Yi, X.; Zheng, A.; Yang, Y. Effect of Coking and Propylene Adsorption on Enhanced Stability for Co^{2+}-catalyzed Propane Dehydrogenation. *J. Catal.* **2021**, *395*, 105−116.
(31) Chen, C.; Zhang, S.; Wang, Z.; Yuan, Z.-Y. Ultrasmall Co Confined in the Silanols of Dealuminated Beta Zeolite: A Highly Active and Selective Catalyst for Direct Dehydrogenation of Propane to Propylene. *J. Catal.* **2020**, *383*, 77−87.
(32) Wang, Y.; Suo, Y.; Ren, J. T.; Wang, Z.; Yuan, Z. Y. Spatially Isolated Cobalt Oxide Sites Derived from MOFs for Direct Propane Dehydrogenation. *J. Colloid Interface Sci.* **2021**, *594*, 113−121.
(33) Bregante, D. T.; Flaherty, D. W. Periodic Trends in Olefin Epoxidation over Group IV and V Framework-Substituted Zeolite Catalysts: A Kinetic and Spectroscopic Study. *J. Am. Chem. Soc.* **2017**, *139*, 6888−6898.
(34) Shamzhy, M.; Opanasenko, M.; Concepción, P.; Martínez, A. New Trends in Tailoring Active Sites in Zeolite-based Catalysts. *Chem. Soc. Rev.* **2019**, *48*, 1095−1149.
(35) Lazić, I.; Bosch, E. G. T.; Lazar, S. Phase Contrast STEM for Thin Samples: Integrated Differential Phase Contrast. *Ultramicroscopy* **2016**, *160*, 265−280.
(36) Lazić, I.; Bosch, E. G. T. Analytical Review of Direct Stem Imaging Techniques for Thin Samples. *Adv. Imaging Electron Phys.* **2017**, *199*, 75−184.
(37) Liu, L.; Wang, N.; Zhu, C.; Liu, X.; Zhu, Y.; Guo, P.; Alfilfil, L.; Dong, X.; Zhang, D.; Han, Y. Direct Imaging of Atomically Dispersed Molybdenum that Enables Location of Aluminum in the Framework of Zeolite ZSM-5. *Angew. Chem., Int. Ed.* **2020**, *59*, 819−825.
(38) Chen, Q.; Dwyer, C.; Sheng, G.; Zhu, C.; Li, X.; Zheng, C.; Zhu, Y. Imaging Beam-Sensitive Materials by Electron Microscopy. *Adv. Mater.* **2020**, *32*, No. e1907619.
(39) Shen, B.; Chen, X.; Wang, H.; Xiong, H.; Bosch, E. G. T.; Lazić, I.; Cai, D.; Qian, W.; Jin, S.; Liu, X.; Han, Y.; Wei, F. A Single-Molecule van der Waals Compass. *Nature* **2021**, *592*, 541−544.
(40) Janas, J.; Shishido, T.; Che, M.; Dzwigaj, S. Role of Tetrahedral Co(II) Sites of CoSiBEA zeolite in the Selective Catalytic Reduction of NO: XRD, UV-vis, XAS and Catalysis Study. *Appl. Catal., B* **2009**, *89*, 196−203.
(41) Cotton, F. A.; Goodgame, M. L.; Goodgame, M. The Electronic Structures of Tetrahedral Cobalt(II) Complexes. *J. Am. Chem. Soc.* **1961**, *83*, 4690−4699.
(42) Harris, J. W.; Cordon, M. J.; Di Iorio, J. R.; Vega-Vila, J. C.; Ribeiro, F. H.; Gounder, R. Titration and Quantification of Open and Closed Lewis Acid Sites in Sn-Beta Zeolites that Catalyze Glucose Isomerization. *J. Catal.* **2016**, *335*, 141−154.
(43) Dubray, F.; Moldovan, S.; Kouvatas, C.; Grand, J.; Aquino, C.; Barrier, N.; Gilson, J. P.; Nesterenko, N.; Minoux, D.; Mintova, S. Direct Evidence for Single Molybdenum Atoms Incorporated in the Framework of MFI Zeolite Nanocrystals. *J. Am. Chem. Soc.* **2019**, *141*, 8689−8693.
(44) Cordon, M. J.; Harris, J. W.; Vega-Vila, J. C.; Bates, J. S.; Kaur, S.; Gupta, M.; Witzke, M. E.; Wegener, E. C.; Miller, J. T.; Flaherty, D. W.; Hibbitts, D. D.; Gounder, R. Dominant Role of Entropy in Stabilizing Sugar Isomerization Transition States within Hydrophobic Zeolite Pores. *J. Am. Chem. Soc.* **2018**, *140*, 14244−14266.
(45) Emeis, C. A. Determination of Intergrated Molar Extincition Coefficients for Infrared Absorption Bands of Pyridine Adsorbed on Solid Acid Catalysts. *J. Catal.* **1993**, *141*, 347−354.
(46) Grand, J.; Talapaneni, S. N.; Vicente, A.; Fernandez, C.; Dib, E.; Aleksandrov, H. A.; Vayssilov, G. N.; Retoux, R.; Boullay, P.; Gilson, J. P.; Valtchev, V.; Mintova, S. One-Pot Synthesis of Silanol-Free Nanosized MFI Zeolite. *Nat. Mater.* **2017**, *16*, 1010−1015.
(47) Zhang, Y.; Qi, L.; Lund, A.; Lu, P.; Bell, A. T. Mechanism and Kinetics of Acetone Conversion to Isobutene over Isolated Hf Sites Grafted to Silicalite-1 and SiO_2. *J. Am. Chem. Soc.* **2021**, *143*, 8352−8366.
(48) Wang, N.; Sun, Q.; Zhang, T.; Mayoral, A.; Li, L.; Zhou, X.; Xu, J.; Zhang, P.; Yu, J. Impregnating Subnanometer Metallic Nanocatalysts into Self-Pillared Zeolite Nanosheets. *J. Am. Chem. Soc.* **2021**, *143*, 6905−6914.
(49) Yan, T.; Dai, W.; Wu, G.; Lang, S.; Hunger, M.; Guan, N.; Li, L. Mechanistic Insights into One-Step Catalytic Conversion of Ethanol to Butadiene over Bifunctional Zn−Y/Beta Zeolite. *ACS Catal.* **2018**, *8*, 2760−2773.
(50) Hu, Z. P.; Weng, C.-C.; Chen, C.; Yuan, Z.-Y. Catalytic Decomposition of Ammonia to CO_x-Free Hydrogen over Ni/ZSM-5 Catalysts: A Comparative Study of the Preparation Methods. *Appl. Catal., A* **2018**, *562*, 49−57.
(51) Otto, T.; Zones, S. I.; Hong, Y.; Iglesia, E. Synthesis of Highly Dispersed Cobalt Oxide Clusters Encapsulated within LTA Zeolites. *J. Catal.* **2017**, *356*, 173−185.
(52) Kim, J.; Lee, S.; Cho, K.; Na, K.; Lee, C.; Ryoo, R. Mesoporous MFI Zeolite Nanosponge Supporting Cobalt Nanoparticles as a

Fischer−Tropsch Catalyst with High Yield of Branched Hydrocarbons in the Gasoline Range. *ACS Catal.* **2014**, *4*, 3919−3927.
(53) Sattler, J. J. H. B.; Ruiz-Martinez, J.; Santillan-Jimenez, E.; Weckhuysen, B. M. Catalytic Dehydrogenation of Light Alkanes on Metals and Metal Oxides. *Chem. Rev.* **2014**, *114*, 10613−10653.
(54) Hu, Z. P.; Yang, D.; Wang, Z.; Yuan, Z.-Y. State-of-the-Art Catalysts for Direct Dehydrogenation of Propane to Propylene. *Chin. J. Catal.* **2019**, *40*, 1233−1254.
(55) Chen, S.; Chang, X.; Sun, G.; Zhang, T.; Xu, Y.; Wang, Y.; Pei, C.; Gong, J. Propane Dehydrogenation: Catalyst Development, New chemistry, and Emerging Technologies. *Chem. Soc. Rev.* **2021**, *50*, 3315−3354.
(56) Li, C.; Wang, G. Dehydrogenation of Light Alkanes to Mono-Olefins. *Chem. Soc. Rev.* **2021**, *50*, 4359−4381.

https://doi.org/10.1021/jacs.2c02636
J. Am. Chem. Soc. 2022, 144, 12127−12137